High-Pressure Stability and Compressibility of Zircon-Type YV$_{1-x}$P$_x$O$_4$:Eu^{3+} Solid-Solution Nanoparticles: An X-ray Diffraction and Raman Spectroscopy Study

Hongsheng Yuan,[†] Kai Wang,[†] Shourui Li,[†] Xiao Tan,[†] Qian Li,[†] Tingting Yan,[†] Ke Yang,[‡] Jing Liu,[§] Bingbing Liu,[†] Guangtian Zou,[†] and Bo Zou*,[†]

[†]State Key Laboratory of Superhard Materials, Jilin University, Changchun 130012, China
[‡]Shanghai Institute of Applied Physics, Chinese Academy of Sciences, Shanghai 201203, China
[§]Beijing Synchrotron Radiation Facility, Institute of High Energy Physics, Chinese Academy of Sciences, Beijing 100049, China

Ⓢ Supporting Information

ABSTRACT: We probed the high-pressure response of the YV$_{1-x}$P$_x$O$_4$:Eu^{3+} (x = 0, 0.5, 0.7, 1.0) solid-solution nanoparticles using angular dispersive synchrotron X-ray diffraction (XRD) and Raman techniques at room temperature. In situ diffraction results showed that the overall nanoparticles underwent an irreversible zircon-to-scheelite structural transformation. The transition pressures were ~9.3, ~12.1, ~14, and ~18.4 GPa for the YV$_{1-x}$P$_x$O$_4$:Eu^{3+} (x = 0, 0.5, 0.7, 1.0) samples, respectively. Coupled with the zircon-to-scheelite transition features, it was proposed that the transition pressure was probably governed by the stiffness of VO$_4$/PO$_4$ units in the solid solutions. This claim was verified by further Raman measurements, which revealed that the stiffness of VO$_4$/PO$_4$ units was enhanced with increasing P contents. The structural refinements showed that the samples with comparable particle size (20−90 nm) became less compressible with increasing P content (x = 0 → 0.7 → 1.0). However, the compressibility of the YV$_{0.5}$P$_{0.5}$O$_4$:Eu^{3+} sample with smaller particle size (10−30 nm) was similar to that of the YV$_{0.3}$P$_{0.7}$O$_4$:Eu^{3+} sample. The general compressibility behavior as a function of P content was ascribed to the special packing style related to the stiffness of VO$_4$/PO$_4$ tetrahedra in zircon structure, and the higher surface energy contribution was responsible for the exceptional compressibility in the smaller nanoparticles.
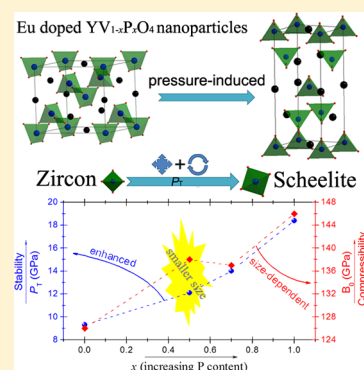
■ INTRODUCTION

Zircon-type ABO$_4$ ternary oxides are common accessory minerals, and they share many physical properties, as well as displaying variable degrees of solid solutions among end members existing in a wide variety of sedimentary, igneous, and metamorphic rocks.[1] The high-pressure research on zircon-type ABO$_4$ compounds has drawn considerable interest in the past several decades because it could provide a wide range of geochemical and geophysical investigations, including studies on the evolution of Earth's crust and mantle.[1,2] Apart from the geophysical importance, the rare-earth orthovanadates RVO$_4$ and orthophosphates RPO$_4$ currently attract considerable interest by virtue of their wide potential applications and interesting optical/luminescent properties.[3−6] They generally crystallize, depending on the ionic radii of the R cation, in two different structural types: zircon [space group (SG): I4$_1$/amd, Z = 4] and monazite [SG: P2$_1$/n, Z = 4]. Those with a small R size ($r_R < r_{La}$ for RVO$_4$ and $r_R < r_{Gd}$ for RPO$_4$) adopt the zircon structure under ambient conditions, whereas the others have the lower-symmetry monoclinic monazite structure.[7−9] Specifically, depending on the growth conditions, GdPO$_4$, TbPO$_4$, DyPO$_4$, and HoPO$_4$ can adopt either zircon or monazite structure.[10] The high-pressure behavior of zircon-type RVO$_4$ and RPO$_4$ compounds was addressed recently. Upon

compression, a direct transition to scheelite structure [SG: I4$_1$/a, Z = 4] occurs in almost all the zircon-type RVO$_4$ compounds except CeVO$_4$, which displays the complete zircon-to-monazite-to-scheelite transition sequence.[11−22] For zircon-type RPO$_4$ compounds, those where the R/P cation size ratio is similar to that of monazite prefer the zircon-to-monazite phase transition; and those where the R/P cation size ratio is similar to that of scheelite prefer the zircon-to-scheelite phase transition.[7,23−27]

Unlike scheelite-type ABO$_4$ compounds in which the transition pressures would increase with the ratio r_{BO_4}/r_A, where r_{BO_4} and r_A present the radii of BO$_4$ units and A-site cation,[28] Errandonea et al. found the zircon-to-scheelite phase transition pressure (P_T) for a specific family of zircon-type ABO$_4$ compounds is quite close and nearly independent of the A cation size.[11] For instance, the P_T for orthovanadates is always around 7−8 GPa,[11,14,20] the P_T for the silicates and phosphates is around 20 GPa,[7,23,27] and that for the chromates is below 6 GPa.[29−31] As Errandonea et al. commented, the

compacted SiO_4 and PO_4 polyhedra probably make the zircon structure more stable, while cooperative interactions between the $3d$ electrons of the transition metals in vanadates and chromates could make the zircon structure less stable upon compression.[11] Systematic investigations, however, still lack the high-pressure behavior of the zircon-type ABO_4 solid-solution system by partly substituting for BO_4 from one family to another, in order to gain further physical insight into zircon structural stability upon compression. Motivated by this, we consider the $YV_{1-x}P_xO_4$ solid-solution system as a significant prototype to investigate the issue due to the big structural stability difference between zircon-type orthovanadates and orthophosphates. Taking into account high-homogeneity, high-purity and precise molar ratio of P to V requirements for the starting materials, the products synthesized by the hydrothermal method could be good options thanks to the recent research efforts on the synthesis of nanophosphors.[3−5]

Herein, we reported the high-pressure response of well-characterized $YV_{1-x}P_xO_4$:Eu^{3+} (x = 0, 0.5, 0.7, 1.0) solid-solution nanoparticles up to 32 GPa at room temperature. By angular dispersive synchrotron X-ray diffraction (XRD), we observed that the overall nanoparticles underwent an irreversible zircon-to-scheelite phase transition and that the P_T increased with the increase in x value. By combining the zircon-to-scheelite transition features with these systematic results, it was proposed that the P_T of zircon-to-scheelite phase transition is probably governed by the stiffness of BO_4 units, and subsequent Raman studies well supported the claim. In addition, a comparative discussion of compressibility was presented for zircon structure in the solid-solution nanoparticles. We believe that the outcomes of this work could deepen the understanding of the zircon-to-scheelite transition nature among the zircon-type ABO_4 compounds and may have wide implications to other high-pressure solid-solution systems.

EXPERIMENTAL SECTION

The $YV_{1-x}P_xO_4$:Eu^{3+} (x = 0, 0.5, 0.7, 1.0) samples (5 mol % Eu) were prepared by a hydrothermal method mostly according to the reported procedure.[3,4] The only difference is that we did not adjust the pH value for the overall samples. Typically, 0.06 mmol of $Y(NO_3)_3$·$6H_2O$ and $Eu(NO_3)_3$·$6H_2O$ was first dissolved in 15 mL of distilled water, and then 20 mL of the mixed solution containing 0.06 mmol of $NaVO_3$·$2H_2O$ and $(NH_4)_2HPO_4$ was added with continuous stirring for 0.5 h. Then, the mixture was transferred into a 50 mL Teflon-lined autoclave. The autoclave was heated to 200 °C for 18 h and cooled to room temperature naturally. The as-prepared $YV_{1-x}P_xO_4$:Eu^{3+} nanocrystals were separated by centrifugation and washed with H_2O twice, followed by drying at 60 °C in air overnight. Powder XRD data under ambient conditions were collected via a Shimadzu XRD-6000 working with a Cu−Kα target. Morphology observation was performed on a JEOL JEM-6700F scanning electron microscope (SEM) and/or a JEM-2200FS transmission electron microscopy (TEM). Photoluminescence (PL) measurements were performed with a Quanta Master 40 spectrometer (produced by Photon Technology Inc.) in reflection mode. The 405 nm line of a violet diode laser with a spot size of 20 μm and a power of 30 mW was used as the excitation source. The typical resolution in the present study was 0.25 nm, and the normalized intensity of all measured peaks in PL spectra was recorded. Raman scattering measurements were carried out using the Renishaw system (inVia Raman microscope) with a 632.8 nm He−Ne

laser as the excitation source. The laser power was 10 mW at the sample, and the integration time was 50 s. The resolution of Raman system was about 1 cm^{-1}.

High-pressure experiments were conducted in a symmetric diamond anvil cell (DAC) furnished with 300 μm culet diamonds at room temperature. The sample was placed in the 110 μm diameter holes of the T301 steel gasket. The 4:1 mixture of methanol and ethanol was used as pressure-transmitting medium. Pressure was determined from the fluorescence spectra of the ruby.[32] In situ XRD experiments with a wavelength of 0.6199 Å and a focused beam size of about 4×7 μm² were performed at beamline 15U1, Shanghai Synchrotron Radiation Facility, China. The XRD patterns were collected for 10 s at each pressure using a Mar-165 CCD detector and then were integrated with FIT2D program.[33] Part of the X-ray diffraction experiments were performed at the 4W2 beamline of Beijing Synchrotron Radiation Facility (BSRF) (wavelength 0.6199 Å, beam size 30 × 30 μm²). A detailed Rietveld analysis was performed using the GSAS software with the graphical EXPGUI user interface.[34]

RESULTS AND DISCUSSION

The XRD patterns of as-prepared samples under ambient conditions are shown in Figure 1a, and the enlarged patterns of

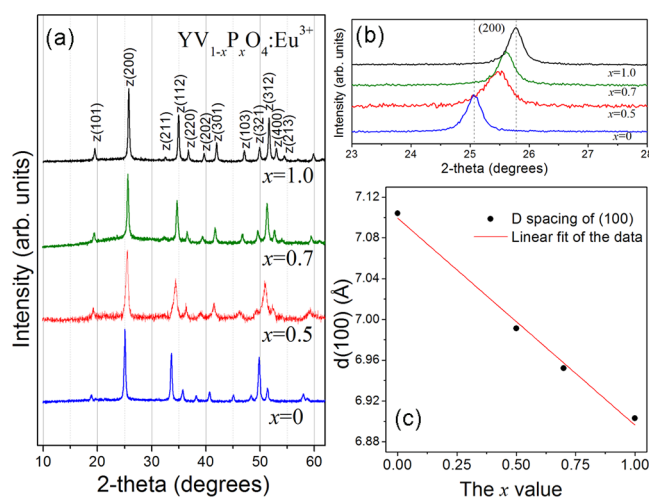**Figure 1.** (a) XRD patterns of the $YV_{1-x}P_xO_4$:Eu^{3+} (x = 0, 0.5, 0.7, 1.0) samples with a Cu−Kα target under ambient conditions. (b) The enlarged patterns of panel a at ~25 degrees attributed to the diffractions (200) in zircon phases. (c) The plot of the unit cell parameter a versus x.

the Bragg peaks (200) are depicted in Figure 1b. The overall XRD patterns conform to the formation of complete solid solutions with single zircon-type structure. The XRD peaks shift toward the higher diffraction angle side from x = 0 to 1.0. This is attributed by the smaller ionic radius of P^{5+}(0.34 Å) than that of V^{5+}(0.59 Å).[3] According to the previous studies, P^{5+} and V^{5+} in the $YV_{1-x}P_xO_4$:Eu^{3+} solid solutions could substitute for each other in any P/V molar ratio.[3,35] Accordingly, the lattice parameters in the solid solutions should be subject to Vegard's law.[3,35] As seen in Figure 1c, the experimental plot of the cell parameter a versus x reveals linear variation, indicating the $YV_{1-x}P_xO_4$:Eu^{3+} samples obey Vegard's law very well. Therefore, it is reasonable to describe the P/V molar ratios on the basis of feed ratios for our samples. Interestingly, the peak width of the $YV_{0.5}P_{0.5}O_4$:Eu^{3+} sample is

somewhat greater than the others, indicative of the smaller particle size. Then the sizes and morphologies were investigated by the SEM images (Figure 2). The overall nanocrystals exhibit
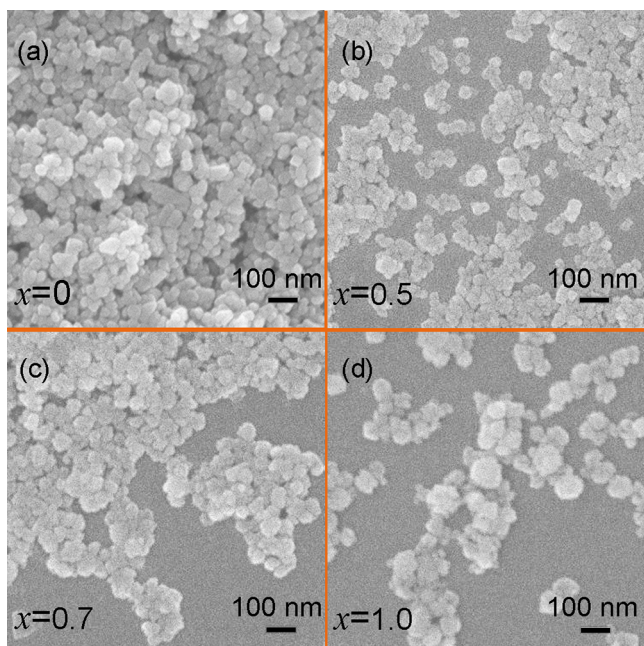

Figure 2. SEM images of the $YV_{1-x}P_xO_4$:Eu^{3+} (x = 0, 0.5, 0.7, 1.0) samples.

Figure 3. PL emission spectra (λ_{ex} = 405 nm) (a) and high-frequency Raman spectra (b) of the $YV_{1-x}P_xO_4$:Eu^{3+} (x = 0, 0.5, 0.7, 1.0) nanoparticles. The dashed lines are guides for the eyes.

particle-like morphology. In contrast with the $YV_{1-x}P_xO_4$:Eu^{3+} (x = 0, 0.7, 1.0) samples, which have comparable particle size in the range of 20 to 90 nm, the $YV_{0.5}P_{0.5}O_4$:Eu^{3+} sample has smaller particle size around 20 nm. Accordingly, two typical samples YVO_4:Eu^{3+} and $YV_{0.5}P_{0.5}O_4$:Eu^{3+} were further characterized by TEM images (Figure S1, Supporting Information). As expected, the TEM images show that $YV_{0.5}P_{0.5}O_4$:Eu^{3+} sample has smaller particle size of 10−30 nm in diameter than the YVO_4:Eu^{3+} sample with 20−90 nm in diameter, nicely correlating with the SEM and XRD results. In fact, it is difficult to gain a series of ideal nanoparticles representing a close average crystallite size with small size dispersions in the solid-solution system. According to the previous synthetic procedure with pH treatment, the nanocrystals would exhibit rod-like morphology when x > 0.6, although the overall $YV_{1-x}P_xO_4$:Eu^{3+} nanocrystals are uniform with ~20 nm in diameter.[3,4] It is suggested that the cooperativity of the pH effect and the P content effect should be responsible for the phenomena, but the specific reason is beyond the scope of the present work. More importantly, the analogous particle-like morphology in present work rules out the possible shape-dependent effect on phase stability, which has been found in the ZnS nanobelts/nanorods, MnS nanobipods, and $CuGaS_2$ nanorods.[36−39] Besides, the smaller particle size of the $YV_{0.5}P_{0.5}O_4$:Eu^{3+} sample offers an opportunity for investigating the cooperativity of size effect and BO_4 substitution effect on the relevant mechanical properties.[40−42]

The overall samples were characterized by PL and Raman spectra further. In the zircon-type $YV_{1-x}P_xO_4$:Eu^{3+} solid solutions, the Eu^{3+} ions replace the Y^{3+} ions with D_{2d} site symmetry. As shown in Figure 3a, group theory predicts four PL peaks from $^5D_0 \rightarrow {}^7F_{1,2}$ transitions. It has been noted that

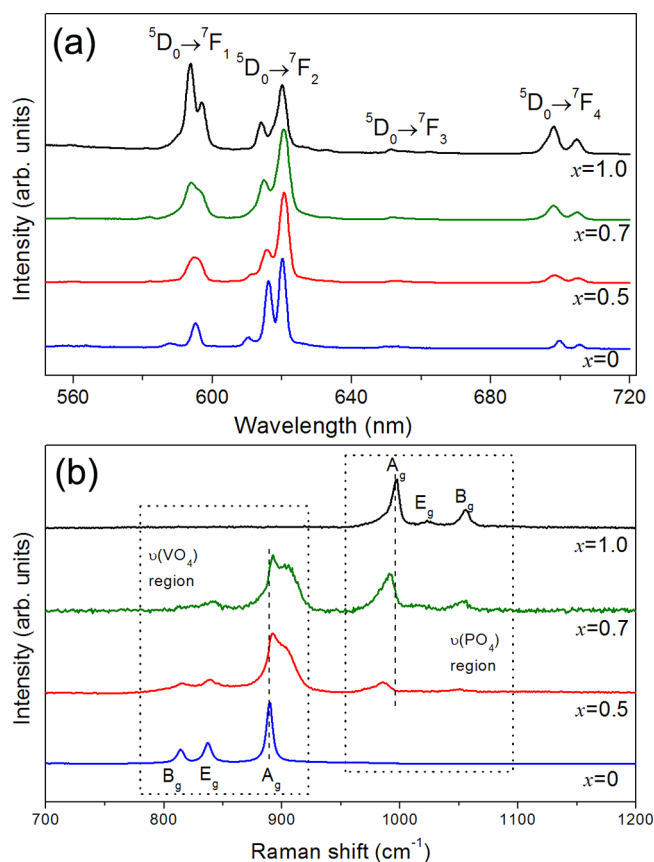the intensity of the $^5D_0 \rightarrow {}^7F_2$ transition becomes greater with increasing polarizability of the surrounding anions.[43] Since the electronegativity of V(1.63) is smaller than that of P(2.19), the polarizability of oxygen anions in Eu^{3+}−O^{2-}−V^{5+} bonds is stronger than that in Eu^{3+}−O^{2-}−P^{5+} bonds.[3] Consequently, the red($^5D_0 \rightarrow {}^7F_2$)-to-orange($^5D_0 \rightarrow {}^7F_1$) intensity ratio deceases with an increasing amount of P, which is consistent with the previous studies.[3,43] The chemical bonding information of V(P)O_4 tetrahedra could be gained by Raman spectra. In particular, the $\nu_1(A_g)$ mode, which represents the V(P)−O bond stretching mode located in the high-frequency range, is highly sensitive to pressure-induced structural transformations. The Raman spectra of the original samples are depicted in Figure 3b. For $YV_{0.5}P_{0.5}O_4$:Eu^{3+} and $YV_{0.3}P_{0.7}O_4$:Eu^{3+} samples, the local structure could a priori differ from the average tetragonal structure due to the random distribution of VO_4 and PO_4 units in the D_{2d} sites, resulting in the deformation and broadening of the V(P)−O bond stretching $\nu_1(A_g)$ mode.[44] Notably, the $\nu_1(A_g)$ mode in both PO_4 and VO_4 units moves to higher-frequency side with the increase in x value, and it is a manifestation of the shortening of the V−O and P−O distances, which comes from the fact that the zircon-type solid solutions are well crystallized by self-adjustments of the PO_4 and VO_4 units.[44] In fact, the Raman mode $\nu(A_{1g})/PO_4$ will be hardly discernible or even disappear when x < 0.5. Likewise, the x value could not be too large for detecting the $\nu(A_{1g})/VO_4$ mode unambiguously. As a matter of course, the YVO_4:Eu^{3+} and YPO_4:Eu^{3+} samples, two extremities in the solid-solution system, merit attention as references. Therefore, the overall
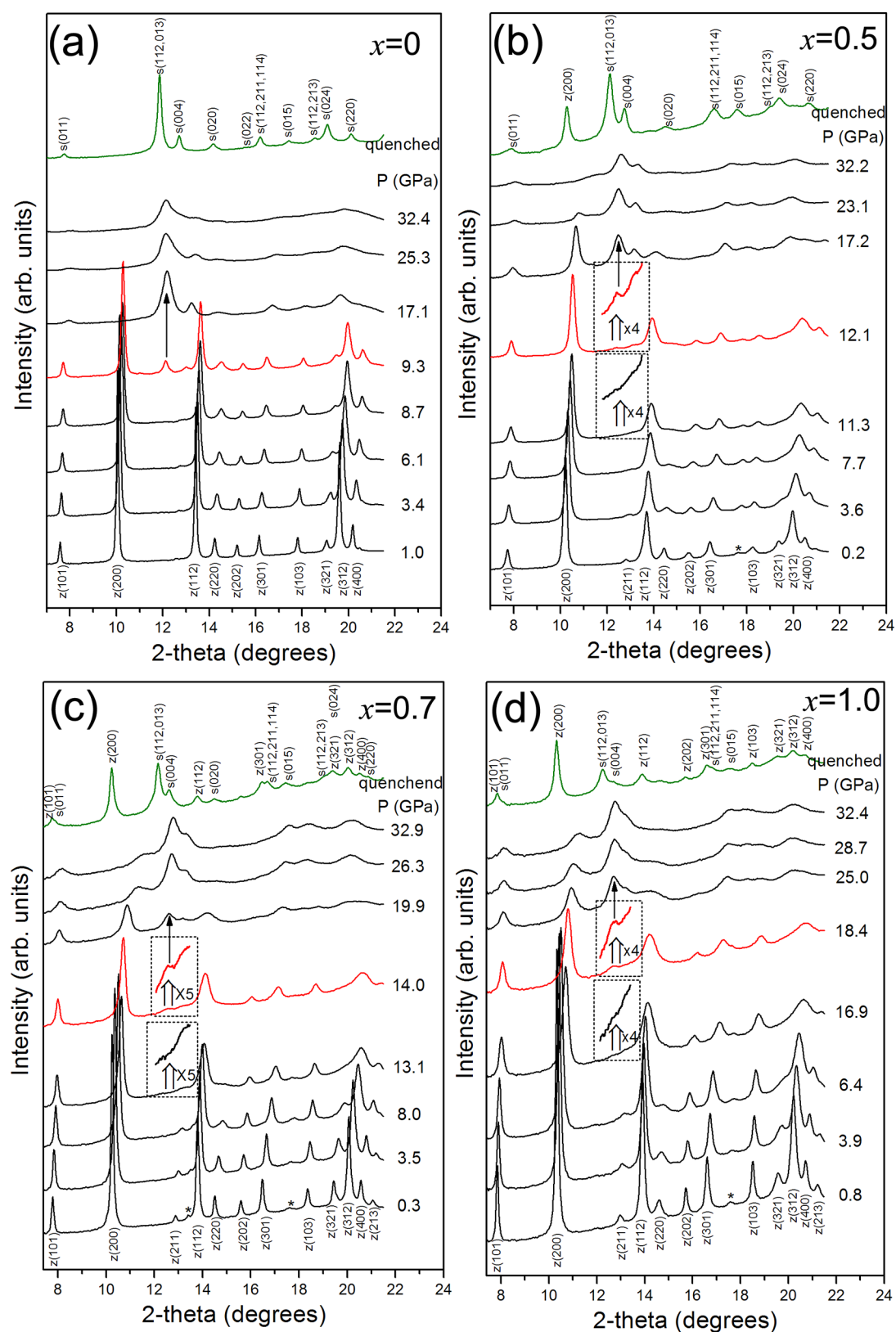
Figure 4. XRD patterns of $YV_{1-x}P_xO_4$:Eu^{3+} ($x = 0, 0.5, 0.7, 1.0$) nanoparticles at various pressures ($\lambda = 0.6199$ Å). The arrows and asterisks denote the Bragg peak (112, 013) attributed to the scheelite structure and the Bragg peak due to the stainless-steel gasket, respectively. The short patterns in panels b, c, and d are parts of the corresponding magnified patterns around phase transition pressures for better observation. Panel d is adapted with permission from ref 27. Copyright 2012 American Chemical Society.

samples $YV_{1-x}P_xO_4$:Eu^{3+} ($x = 0, 0.5, 0.7, 1.0$) were selected meticulously into this solid-solution system for fully character-

ization and comparison. In short, we could confirm that the starting materials are the single-phase zircon-type

$YV_{1-x}P_xO_4$:Eu^{3+} solid-solution nanoparticles with the premeditated element proportion by utilizing the XRD, SEM, TEM, PL, and Raman techniques.

The high-pressure XRD experiments were conducted on the well-characterized nanoparticles with the attainable highest pressures up to 32 GPa for the purpose of parallel comparison. The selected powder XRD patterns of the solid-solution nanoparticles at various pressures are shown in Figure 4. With the increase in pressure, a new Bragg peak marked with the arrow appears clearly in each panel for the corresponding samples, which indicates the onset of the phase transition. For bulk YVO_4 compounds upon compression, an irreversible zircon-to-scheelite phase transition has been investigated by XRD technique with the P_T at 8.5 GPa,[20] and a reversible phase transition from scheelite phase to M-fergusonite phase has been detected at ~20 GPa by Raman measurements.[15] The direct zircon-to-scheelite phase transition without going through monazite structure in the YPO_4 nanoparticles (with and without Eu^{3+} doping) has been convinced by high-pressure XRD and PL measurements in our recent work, and it was proposed that the nanoscale-induced higher surface energy contribution plays a crucial role in the distinctive high-pressure behavior of the nanoparticles compared with the bulk.[27] We would like to declare that the experimental data of YPO_4:Eu^{3+} nanoparticles are reused from our recent work in ref 27. In view of this, the new Bragg peak for each sample could be readily indexed as the strongest diffraction maxima of Bragg peak (112, 013) of the scheelite structure, indicative of the zircon-to-scheelite phase transition under high pressure. The P_T of zircon-to-scheelite phase transition could be determined from the XRD patterns as follows: ~9.3 GPa for YVO_4:Eu^{3+}; ~12.1 GPa for $YV_{0.5}P_{0.5}O_4$:Eu^{3+}; ~14 GPa for $YV_{0.3}P_{0.7}O_4$:Eu^{3+}; and ~18.4 GPa for YPO_4:Eu^{3+} samples. We could not determine the phase transition from scheelite phase to M-fergusonite phase by our XRD experiments on YVO_4:Eu^{3+} nanoparticles due to the serious Bragg peak broadening at higher pressures. Furthermore, the most pronounced Bragg peak (200) in zircon phase could be still detected in $YV_{1-x}P_xO_4$:Eu^{3+} (x = 0.5, 0.7, 1.0) samples at the attainable highest pressures 32 GPa. By the return to ambient pressure, the scheelite phase is reserved in the quenched samples, which is important for design and fabrication of novel materials with tailed properties.[42,45] The proportion of the original zircon phase and high-pressure scheelite phase in the quenched samples can be qualitatively identified by the relative intensity of the Bragg peak (200) for zircon phase and the Bragg peak (112, 013) for scheelite phase, and hence, it is found that the content of the scheelite phase in the quenched samples (completely decompressed from 32 GPa) is declined with increasing P content.

According to the previous results, Errandonea et al. concluded that the zircon-to-scheelite phase transition pressure (high-pressure zircon structural stability) is strongly related to the composition of BO_4 units in zircon-type ABO_4 compounds.[11] It is noteworthy that the P_T is strongly dependent on the P content in the $YV_{1-x}P_xO_4$:Eu^{3+} solid-solution nanoparticles, despite of the smaller particle size found in the $YV_{0.5}P_{0.5}O_4$:Eu^{3+} sample. Therefore, subsequent analysis and Raman experiments on these solid-solution nanoparticles were performed to further investigate this issue.

It is accepted that the higher symmetry of zircon structure hinders the rotation of BO_4 tetrahedra, while the scheelite structure is flexible where the rotation of BO_4 units is allowed.[46] Therefore, the elimination of structural voids among polyhedra

could be adopted by rotation of BO_4 units in scheelite structure, resulting in more efficient crystal packing to accommodate the increasing repulsive and steric stresses induced by pressure. Notably, an abnormal discontinuous decrease of the B–O bond strength is correlated with the zircon-to-scheelite phase transition for all the corresponding zircon-type ABO_4 compounds.[11,15,20,23] Namely, the BO_4 units are expanded to a certain extent accompanied by the rotation of the BO_4 units at the structural transition. Therefore, it is reasonable to regard the expansion of BO_4 units as a prerequisite to trigger the zircon-to-scheelite phase transition under pressure. As such, we propose that the P_T of zircon-to-scheelite phase transition is probably governed by the stiffness of BO_4 units. The proposed principle of zircon-to-scheelite structural transformation in terms of the BO_4 stiffness–P_T relationship is depicted in Figure 5. Additionally, it has also
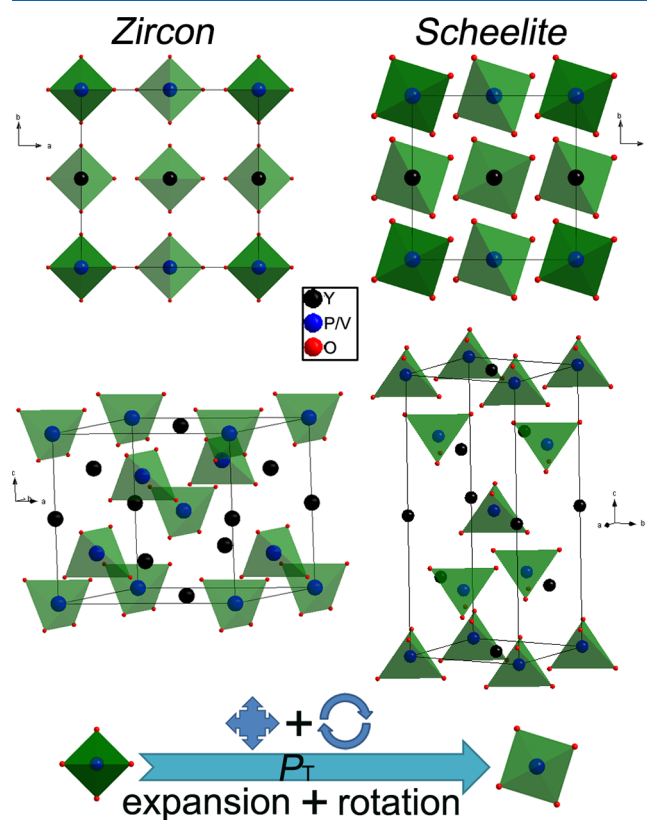

Figure 5. Zircon-type crystal structure of $YV_{1-x}P_xO_4$ at ambient conditions [left, SG: $I4_1/amd$, Z = 4] and the high-pressure scheelite-type structure [right, SG: $I4_1/a$, Z = 4]. In both phases, the V(P) ions are tetrahedrally coordinated, but with different bond lengths and angles. The Y ions are in distorted dodecahedral (8-fold) coordination. To better illustrate the relative arrangement of cations, the origins of the unit cells are chosen at V(P) positions.

been evidenced experimentally that the B–O distance was slightly decreased or even remains nearly constant under pressure in the zircon phase, and the same can be concluded for the scheelite phase.[15,20] Therefore, further Raman measurements were carried out on the quenched samples to verify the claim we proposed.

The Raman spectra of the original and quenched samples regarding the V(P)–O bond stretching mode $\nu_1(A_g)$ are shown in Figure 6. It can be found that the discontinuous changes of the PO_4 and VO_4 units are not isolated but closely connected in
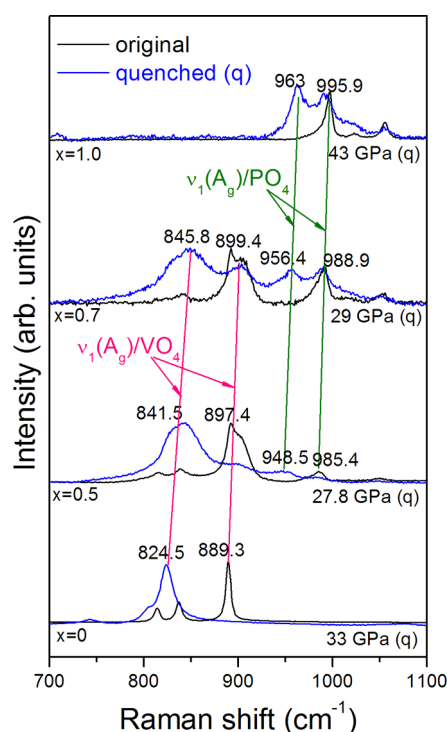
Figure 6. Raman spectra of the original (black) and quenched (blue) $YV_{1-x}P_xO_4:Eu^{3+}$ (x = 0, 0.5, 0.7, 1.0) samples from corresponding pressure. The Raman spectra for $YPO_4:Eu^{3+}$ nanoparticles are adapted with permission from ref 27. Copyright 2012 American Chemical Society.

the solid-solution system. As seen in Figure 6, one/two new mode(s) can be detected obviously in the Raman spectra of the quenched samples, which can be readily assigned to the $\nu_1(A_g)$ mode(s) of the scheelite phase. It could be estimated through a simple calculation from the expression for the force constant κ because $\nu = 1/2\pi \ (\kappa/m)^{1/2}$ and $\nu_a^2/\nu_b^2 \approx \kappa_a/\kappa_b$. Therefore, squaring the frequencies and taking their ratio gives a measure

of the change in the force constant, which is directly related to the change in the bond strength.[21] In going from zircon to scheelite structure, according to the calculation, the V−O bond strength will decrease by ~14%, ~12%, and ~11.5% in $YVO_4:Eu^{3+}$, $YV_{0.5}P_{0.5}O_4:Eu^{3+}$, and $YV_{0.3}P_{0.7}O_4:Eu^{3+}$ samples, respectively; the P−O bond strength will decrease by 7.3%, 6.5%, and 6.5% in $YV_{0.5}P_{0.5}O_4:Eu^{3+}$, $YV_{0.3}P_{0.7}O_4:Eu^{3+}$, and $YPO_4:Eu^{3+}$ samples, respectively (see Table 1). The more dramatic changes of the V(P)−O bond strength imply the diminished ability to resist deformation for the VO_4/PO_4 units in going from zircon to scheelite structure. Theoretically, the bulk modulus of the P−O bond (726 GPa in YPO_4) is much larger than that of the V−O bond (485.4 GPa in YVO_4).[8,9] As a consequence, it is reasonable to conclude that the stiffness of the VO_4/PO_4 units can be improved with increasing P content. The results support the claim that zircon-to-scheelite phase transition pressure is governed by the stiffness of BO_4 units.

To further verify whether the claim could be extended to other similar ABO_4 compounds, we checked the previous valuable Raman results on the corresponding zircon-type ABO_4 ternary oxides upon compression and listed the typical results in Table 1. According to the aforementioned calculation, the estimated bond strength decrease could also be demonstrated in the table. It can be noticed that the close P_T for a specific family of zircon-type ABO_4 compounds is generally associated with similar changes of the B−O bond strength. Across different kinds of BO_4 units, it is indicated that the stiffer the BO_4 units are, the greater the P_T of the zircon-to-scheelite phase transition will get. However, there is an exception for the $YCrO_4$, where the P_T of the zircon-to-scheelite phase transition is only 3 GPa, much lower than the P_T at 6 GPa in the $CaCrO_4$. Notably, there is still one $3d^1$ electron in the outer shell of Cr^{5+} ion in $YCrO_4$, while the electronic distribution is $3d^04s^0$ for Cr^{6+}/V^{5+} and $3s^03p^0$ for P^{5+} in other compounds listed in Table 1. It is widely accepted that the changes of the bond strength could also be attributed to a charge transfer effect.[21] Consequently, the P_T of the zircon-to-scheelite phase transition could be reduced in the $YCrO_4$ by virtue of the contribution

Table 1. Summary of the Typical Experimental Raman Bond Stretching Frequencies $\nu_1(A_g)$ (cm^{-1}) from the Reported/Current (P_T Verified by Raman/XRD) Zircon-Type ABO_4 Compounds by High-Pressure Raman Scattering Measurements under Ambient Conditions and from the Quenched Samples; the Pressure-Transmitting Medium is 4:1 Methanol−Ethanol in the Overall Compounds[a]

		$\nu_1(A_G)$ (cm^{-1})			
compounds	P_T (GPa)	zircon-type phase	scheelite-type phase	estimated bond strength decrease	refs
$LuVO_4$(B)	8.0	901/VO$_4$	830/VO$_4$	~15%/V−O	16
$YbVO_4$(B)	5.9	901/VO$_4$	823/VO$_4$	~16.6%/V−O	17
$DyVO_4$(B)	6.5	889/VO$_4$	825/VO$_4$	~13.9%/V−O	19
$TbVO_4$(B)	6.6	882/VO$_4$	829/VO$_4$	~11.7%/V−O	19
$GdVO_4:Eu^{3+}$(B)	7.4	884/VO$_4$	830/VO$_4$	~11.8%/V−O	14
YVO_4(B)	7.5	891/VO$_4$	828/VO$_4$	~13.6%/V−O	21
$TmPO_4$(B)	20	1006/PO$_4$	980/PO$_4$	~5.1%/P−O	23
$YCrO_4$(B)	3	863/CrO$_4$	804/CrO$_4$	~13%/Cr−O	30
$CaCrO_4$(B)	6	911/CrO$_4$	850/CrO$_4$	~13%/Cr−O	29
$YVO_4:Eu^{3+}$(Nps)	9.3	889.3/VO$_4$	824.5/VO$_4$	~14%/V−O	this work
$YV_{0.5}P_{0.5}O_4:Eu^{3+}$(Nps)	12	897.4/VO$_4$	841.5/VO$_4$	~12%/V−O	this work
		985.4/PO$_4$	948.5/PO$_4$	~7.3%/P−O	
$YV_{0.3}P_{0.7}O_4:Eu^{3+}$(Nps)	14	899.4/VO$_4$	845.8/VO$_4$	~11.5%/V−O	this work
		988.9/PO$_4$	956.4/PO$_4$	~6.5%/P−O	
$YPO_4:Eu^{3+}$(Nps)	18.4	995.9/PO$_4$	963/PO$_4$	~6.5%/P−O	27

[a]B, bulk samples; Nps, nanoparticles.

from the special electronic configuration. As a whole, the Raman results are consistent with the claim that the BO_4 stiffness governs the P_T of zircon-to-scheelite phase transition. Specifically, the stiffer BO_4 units could make the zircon structure more stable.

In contrast with the $YVO_4:Eu^{3+}$ nanoparticles, the zircon-to-scheelite phase transition is sluggish for the other component nanoparticles, and the content of scheelite phase in the quenched samples declines with the increase in the x value accordingly. In our view, the stiffness of $V(P)O_4$ units should also be responsible for this transition sluggishness because more PO_4 substitution for VO_4 units makes the tetrahedra stiffer, resulting in tougher conditions to expand and rotate the tetrahedrons completely through compression. The same can be concluded for RPO_4 compounds in which it is difficult to get a single high-pressure scheelite phase at room temperature.[25,27]

Here, we analyze the compressibility by performing Rietveld refinements. Since the $YV_{1-x}P_xO_4:Eu^{3+}$ solid solutions are isomorphic, we adopted the atom positional parameters of zircon-type YPO_4 crystal for the $YV_{1-x}P_xO_4:Eu^{3+}$ ($x = 0.5, 0.7, 1.0$) samples. The attempts to refine the mixture of zircon and scheelite patterns were unsuccessful because of the serious peak broadening after phase transition. Similarly, we could not refine the XRD patterns at 15.4 and 16.9 GPa in $YPO_4:Eu^{3+}$ very well within experimental error. As a consequence, the profiles before the phase transition were refined for the $YV_{1-x}P_xO_4:Eu^{3+}$ ($x = 0, 0.5, 0.7$) samples; the profiles before 14 GPa were totally refined for the $YPO_4:Eu^{3+}$ sample. The refinement process is introduced in Figures S2–S4, Supporting Information. Figure 7 shows the typical refinements for $YV_{0.5}P_{0.5}O_4:Eu^{3+}$ at 4.8 GPa and $YV_{0.3}P_{0.7}O_4:Eu^{3+}$ at 5.6 GPa. As can be seen in this figure, the agreement between the observed and the calculated pattern is good for both samples.

The pressure dependence of the decreasing a and c lattice parameters and axial ratio c/a are depicted in Figures 8 and 9, respectively. The detailed data are summarized in Table S1, Supporting Information. It is interesting to note that the compression of the zircon-type structure is anisotropic for the overall samples, with the c axis being the less compressible axis, resulting in the increasing axial ratio c/a. The origin of this anisotropic behavior is related to the packing of YO_8 and VO_4/PO_4 polyhedra in the zircon structure. Specifically, the zircon structure consists of isolated VO_4/PO_4 tetrahedra, which surround the Y atom to form YO_8 triangular dodecahedra. The principal structural unit is a chain of alternating VO_4/PO_4 and YO_8 polyhedra extending parallel to the c axis, with the chain joined along the a axis by edge-sharing YO_8 dodecahedra. The fact that the VO_4/PO_4 tetrahedra behave much stiffer than the YO_8 dodecahedra makes the c axis less compressible than the a axis as observed in our experiments. A similar behavior was found in other zircon-type ABO_4 compounds, such as $YAsO_4$ and $YCrO_4$.[31] Furthermore, the general trend is that the samples would become less compressible with increasing P content ($x = 0 \rightarrow 0.7 \rightarrow 1.0$). In particular, the compressibility of the c axis as a function of P content varies more markedly than that of the a axis. This result is in accordance with our claim that the stiffness of VO_4/PO_4 units (parallel to the c axis) is apparently enhanced with increasing P content. An exception to this systematic behavior is the $YV_{0.5}P_{0.5}O_4:Eu^{3+}$ sample, which exhibits similar compressibility in comparison with the $YV_{0.3}P_{0.7}O_4:Eu^{3+}$ sample. Since the average particle size of the $YV_{0.5}P_{0.5}O_4:Eu^{3+}$ sample (10−30 nm) is smaller than other component samples (20−90 nm), this exceptional compressi-
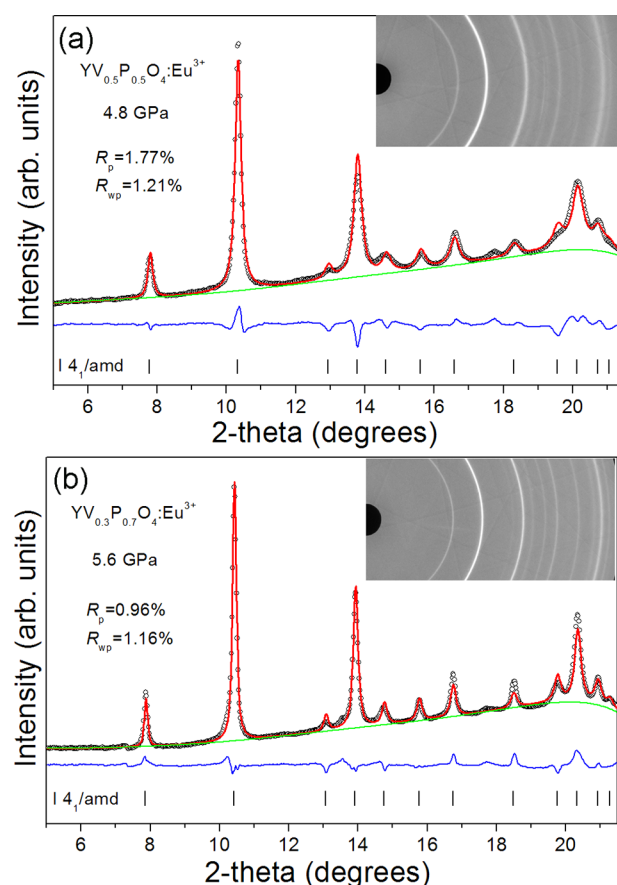

Figure 7. Rietveld refinements for the zircon phase of the $YV_{0.5}P_{0.5}O_4:Eu^{3+}$ (a) and $YV_{0.3}P_{0.7}O_4:Eu^{3+}$ (b) nanoparticles at 4.8 and 5.6 GPa, respectively. The insets represent corresponding diffraction images.
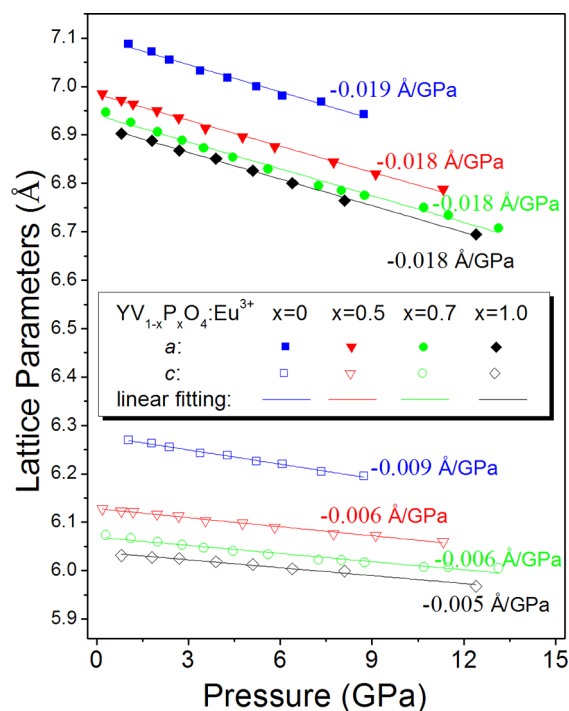

Figure 8. Lattice parameters for the zircon phases of the overall solid-solution nanoparticles as a function of pressure.
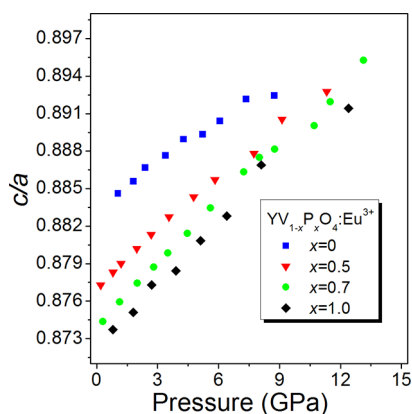
Figure 9. Axial ratios c/a for the zircon phases of the overall solid-solution nanoparticles as a function of pressure.

bility can be rationalized by taking into account the higher surface energy contribution in the smaller nanoparticles, which is in agreement with numerous studies on nanosized materials.[40,41]

From the pressure dependence of the unit-cell parameters, the unit-cell volumes of zircon phase for the four samples as a function of pressure were calculated. A summary can be found in Figure 10. By fitting the third-order Birch–Murnaghan
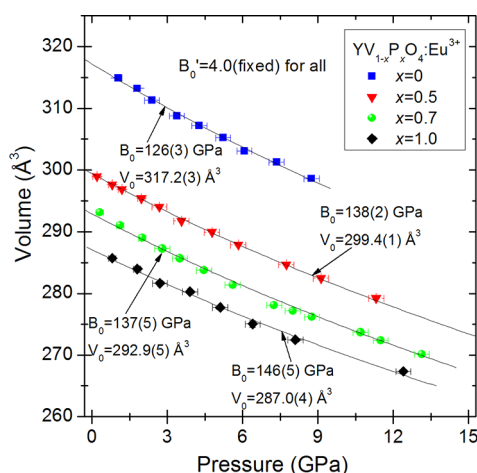

Figure 10. Volume–pressure data for the zircon phases of the overall solid-solution nanoparticles.

equation of state, the corresponding results for zircon structure are also given. It can be found that the bulk modulus (B_0) is elevated with increasing P content, while the B_0 of the $YV_{0.5}P_{0.5}O_4$:Eu^{3+} sample ($\sim$138 GPa) is close to that of the $YV_{0.3}P_{0.7}O_4$:Eu^{3+} sample ($\sim$137 GPa). Additionally, the B_0 for YVO_4:Eu^{3+} nanoparticles ($\sim$126 GPa) and YPO_4:Eu^{3+} nanoparticles ($\sim$146 GPa) are similar to their bulk counterparts ($\sim$130 GPa for bulk YVO_4 and $\sim$149 GPa for bulk YPO_4),[7,20] hinting that further decrease in particle size ($<$20 nm) would result in obvious elevation of bulk modulus compared with their bulk counterparts in the $YV_{1-x}P_xO_4$:Eu^{3+} solid-solution system. On the basis of the results and discussion, it can be suggested that BO_4 substitution in conjunction with size control could be used as an efficient tool for mechanical-properties manipulation in an ABO_4 solid-solution system with other tailored properties.

CONCLUSIONS

In summary, we studied the high-pressure response of the $YV_{1-x}P_xO_4$:Eu^{3+} (x = 0, 0.5, 0.7, 1.0) solid-solution nanoparticles up to 32 GPa at room temperature. By in situ XRD method, we observed that the overall nanoparticles underwent an irreversible zircon-to-scheelite phase transition with the P_T at $\sim$9.3, $\sim$12.1, $\sim$14, and $\sim$18.4 GPa for the $YV_{1-x}P_xO_4$:Eu^{3+} (x = 0, 0.5, 0.7, 1.0) nanoparticles, respectively. We proposed that the P_T of zircon-to-scheelite phase transition was governed by the stiffness of BO_4 units in zircon-type ABO_4 compounds, and subsequent Raman spectra supported the claim. By refinements of the XRD patterns, we found that the samples with comparable particle size (20–90 nm) became less compressible with increasing P content (x = 0 → 0.7 → 1.0), while the $YV_{0.5}P_{0.5}O_4$:Eu^{3+} sample with smaller particle size (10–30 nm) exhibited similar compressibility in comparison with the $YV_{0.3}P_{0.7}O_4$:Eu^{3+} sample. The general compressibility behavior is ascribed to the special packing style in zircon structure related to the stiff VO_4/PO_4 tetrahedra, and the higher surface energy contribution is responsible for the exceptional compressibility in the smaller nanoparticles. This study could deepen the understanding of the zircon-to-scheelite transition nature among the zircon-type ABO_4 compounds. We believe that more studies on the ABO_4 solid solutions are of great importance for getting a systemically complete picture of the phase transition nature on these important materials, which have many implications for the fields including technological applications and Earth and planetary sciences.

ASSOCIATED CONTENT

S Supporting Information
TEM images of YVO_4:Eu^{3+} and $YV_{0.5}P_{0.5}O_4$:Eu^{3+} samples (Figure S1). Typical refinement process (Figures S2−S4). The refined lattice parameters (a,c) and unit volume (V) of zircon structure for the overall samples at various pressures (Table S1). This material is available free of charge via the Internet at http://pubs.acs.org.

AUTHOR INFORMATION

Corresponding Author
*(B.Z.) E-mail: zoubo@jlu.edu.cn.. Phone: 86-431-85168882. Fax: 86-431-85168883.

Notes
The authors declare no competing financial interest.

ACKNOWLEDGMENTS

REFERENCES

(1) Finch, R. J.; Hanchar, J. M. Structure and Chemistry of Zircon and Zircon-Group Minerals. *Rev. Miner. Geochem.* **2003**, *53*, 1−25.

(2) Errandonea, D.; Javier Manjón, F. Pressure Effects on the Structural and Electronic Properties of ABX(4) Scintillating Crystals. *Prog. Mater. Sci.* **2008**, *53*, 711−773.

(3) Zhu, H. L.; Yang, H.; Jin, D. L.; Wang, Z. K.; Gu, X. Y.; Yao, X. H.; Yao, K. H. Hydrothermal Synthesis and Photoluminescent Properties of $YV_{1-x}P_xO_4:Eu^{3+}$ ($x = 0−1.0$) Nanophosphors. *J. Nanopart. Res.* **2008**, *10*, 1149−1154.

(4) Zhu, H. L.; Zuo, D. T. Highly Enhanced Photoluminescence from $YVO_4:Eu^{3+}@YPO_4$ Core/Shell Heteronanostructures. *J. Phys. Chem. C* **2009**, *113*, 10402−10406.

(5) Zhou, J. C.; Sun, L. D.; Shen, J.; Gu, J. Q.; Yan, C. H. Fluorescent-Magnetic Nanocrystals: Synthesis and Property of $YV_{1-x}P_xO_4:Eu^{3+}@GdPO_4$ Core/Shell Structure. *Nanoscale* **2011**, *3*, 1977−1983.

(6) Luwang, M. N.; Ningthoujam, R.; Srivastava, S.; Vatsa, R. Disappearance and Recovery of Luminescence in Bi^{3+}, Eu^{3+} Codoped YPO_4 Nanoparticles Due to the Presence of Water Molecules Up to 800 °C. *J. Am. Chem. Soc.* **2011**, *133*, 2998−3004.

(7) Lacomba-Perales, R.; Errandonea, D.; Meng, Y.; Bettinelli, M. High-Pressure Stability and Compressibility of APO_4 (A = La, Nd, Eu, Gd, Er, and Y) Orthophosphates: An X-ray Diffraction Study Using Synchrotron Radiation. *Phys. Rev. B* **2010**, *81*, 064113−1−064113−9.

(8) Zhang, S.; Zhou, S.; Li, H.; Li, L. Investigation of Thermal Expansion and Compressibility of Rare-Earth Orthovanadates Using a Dielectric Chemical Bond Method. *Inorg. Chem.* **2008**, *47*, 7863−7967.

(9) Li, H. Y.; Zhang, S. Y.; Zhou, S. H.; Cao, X. Q. Bonding Characteristics, Thermal Expansibility, and Compressibility of RXO_4 (R = Rare Earths, X = P, As) within Monazite and Zircon Structures. *Inorg. Chem.* **2009**, *48*, 4542−4548.

(10) Kolitsch, U.; Holtstam, D. Crystal Chemistry of $REEXO_4$ Compounds (X = P, As, V). II. Review of $REEXO_4$ Compounds and Their Stability Fields. *Eur. J. Mineral.* **2004**, *16*, 117−126.

(11) Errandonea, D.; Lacomba-Perales, R.; Ruiz-Fuertes, J.; Segura, A.; Achary, S. N.; Tyagi, A. K. High-Pressure Structural Investigation of Several Zircon-Type Orthovanadates. *Phys. Rev. B* **2009**, *79*, 184104−1−184104−9.

(12) Errandonea, D.; Kumar, R. S.; Achary, S. N.; Tyagi, A. K. In Situ High-Pressure Synchrotron X-Ray Diffraction Study of $CeVO_4$ and $TbVO_4$ up to 50 GPa. *Phys. Rev. B* **2011**, *84*, 224121.

(13) Panchal, V.; López-Moreno, S.; Santamaría-Perez, D.; Errandonea, D.; Manjón, F. J.; Rodríguez-Hernández, P.; Muñoz, A.; Achary, S. N.; Tyagi, A. K. Zircon to Monazite Phase Transition in $CeVO_4$: X-Ray Diffraction and Raman-Scattering Measurements. *Phys. Rev. B* **2011**, *84*, 024111.

(14) Zhang, C. C.; Zhang, Z. M.; Dai, R. C.; Wang, Z. P.; Zhang, J. W.; Ding, Z. J. High-Pressure Raman and Luminescence Study on the Phase Transition of $GdVO_4:Eu^{3+}$ Microcrystals. *J. Phys. Chem. C* **2010**, *114*, 18279−18282.

(15) Manjón, F. J.; Rodríguez-Hernández, P.; Muñoz, A.; Romero, A. H.; Errandonea, D.; Syassen, K. Lattice Dynamics of YVO_4 at High Pressures. *Phys. Rev. B* **2010**, *81*, 075202.

(16) Rao, R.; Garg, A. B.; Sakuntala, T.; Achary, S.; Tyagi, A. High Pressure Raman Scattering Study on the Phase Stability of $LuVO_4$. *J. Solid State Chem.* **2009**, *182*, 1879−1883.

(17) Garg, A. B.; Rao, R.; Sakuntala, T.; Wani, B.; Vijayakumar, V. Phase Stability of $YbVO_4$ Under Pressure: In Situ X-Ray and Raman Spectroscopic Investigations. *J. Appl. Phys.* **2009**, *106*, 063513.

(18) Chen, G.; Stump, N.; Haire, R.; Peterson, J.; Abraham, M. Pressure-Induced Phase Transition in $YVO_4:Eu^{3+}$: A Luminescence Study at High Pressure. *J. Phys. Chem. Solids* **1992**, *53*, 1253−1257.

(19) Duclos, S. J.; Jayaraman, A.; Espinosa, G.; Cooper, A.; Maines, R., Sr. Raman and Optical Absorption Studies of the Pressure-Induced Zircon to Scheelite Structure Transformation in $TbVO_4$ and $DyVO_4$. *J. Phys. Chem. Solids* **1989**, *50*, 769−775.

(20) Wang, X.; Loa, I.; Syassen, K.; Hanfland, M.; Ferrand, B. Structural Properties of the Zircon- and Scheelite-Type Phases of YVO_4 at High Pressure. *Phys. Rev. B* **2004**, *70*, 064109.

(21) Jayaraman, A.; Kourouklis, G.; Espinosa, G.; Cooper, A.; Van Uitert, L. A High-Pressure Raman Study of Yttrium Vanadate (YVO_4) and the Pressure-Induced Transition from the Zircon-Type to the Scheelite-Type Structure. *J. Phys. Chem. Solids* **1987**, *48*, 755−759.

(22) Huang, Z. C.; Zhang, L.; Pan, W. Synthesis, Lattice Dynamics, and Mechanical Properties of a High-Pressure Scheelite Phase of RVO_4. *Inorg. Chem.* **2012**, *51*, 11235−11237.

(23) Stavrou, E.; Tatsi, A.; Raptis, C.; Efthimiopoulos, I.; Syassen, K.; Muñoz, A.; Rodríguez-Hernández, P.; López-Solano, J.; Hanfland, M. Effects of Pressure on the Structure and Lattice Dynamics of $TmPO_4$: Experiments and Calculations. *Phys. Rev. B* **2012**, *85*, 024117.

(24) López-Solano, J.; Rodríguez-Hernández, P.; Muñoz, A.; Gomis, O.; Santamaría-Perez, D.; Errandonea, D.; Manjón, F. J.; Kumar, R. S.; Stavrou, E.; Raptis, C. Theoretical and Experimental Study of the Structural Stability of $TbPO_4$ at High Pressures. *Phys. Rev. B* **2010**, *81*, 144126.

(25) Zhang, F. X.; Wang, J. W.; Lang, M.; Zhang, J. M.; Ewing, R. C.; Boatner, L. A. High-Pressure Phase Transitions of $ScPO_4$ and YPO_4. *Phys. Rev. B* **2009**, *80*, 184114.

(26) Zhang, F. X.; Lang, M.; Ewing, R. C.; Lian, J.; Wang, Z. W.; Hu, J.; Boatner, L. A. Pressure-Induced Zircon-Type to Scheelite-Type Phase Transitions in $YbPO_4$ and $LuPO_4$. *J. Solid State Chem.* **2008**, *181*, 2633−2638.

(27) Yuan, H. S.; Wang, K.; Li, S. R.; Tan, X.; Li, Q.; Yan, T. T.; Cheng, B. Y.; Yang, K.; Liu, B. B.; Zou, G. T.; et al. Direct Zircon-to-Scheelite Structural Transformation in YPO_4 and $YPO_4:Eu^{3+}$ Nanoparticles under High Pressure. *J. Phys. Chem. C* **2012**, *116*, 24837−24844.

(28) Errandonea, D.; Manjón, F.; Somayazulu, M.; Häusermann, D. Effects of Pressure on the Local Atomic Structure of $CaWO_4$ and $YLiF_4$: Mechanism of the Scheelite-to-Wolframite and Scheelite-to-Fergusonite Transitions. *J. Solid State Chem.* **2004**, *177*, 1087−1097.

(29) Long, Y. W.; Zhang, W. W.; Yang, L. X.; Yu, Y.; Yu, R. C.; Ding, S.; Liu, Y. L.; Jin, C. Q. Pressure-Induced Structural Phase Transition in $CaCrO_4$: Evidence from Raman Scattering Studies. *Appl. Phys. Lett.* **2005**, *87*, 181901−1−181901−3.

(30) Long, Y. W.; Yang, L. X.; Yu, Y.; Li, F. Y.; Yu, R. C.; Ding, S.; Liu, Y. L.; Jin, C. Q. High-Pressure Raman Scattering and Structural Phase Transition in $YCrO_4$. *Phys. Rev. B* **2006**, *74*, 054110.

(31) Errandonea, D.; Kumar, R.; López-Solano, J.; Rodríguez-Hernández, P.; Muñoz, A.; Rabie, M. G.; Sáez Puche, R. Experimental and Theoretical Study of Structural Properties and Phase Transitions in $YAsO_4$ and $YCrO_4$. *Phys. Rev. B* **2011**, *83*, 134109.

(32) Mao, H. K.; Xu, J.; Bell, P. Calibration of the Ruby Pressure Gauge to 800 kbar Under Quasi-Hydrostatic Conditions. *J. Geophys. Res.* **1986**, *91*, 4673−4676.

(33) Hammersley, A.; Svensson, S.; Hanfland, M.; Fitch, A.; Hausermann, D. Two-Dimensional Detector Software: From Real Detector to Idealised Image or Two-Theta Scan. *High Pressure Res.* **1996**, *14*, 235−248.

(34) Larson, A. C.; Von Dreele, R. B. General Structure Analysis System (GSAS). *Los Alamos National Laboratory Report LAUR*, 2004; Report Number 86748.

(35) Ropp, R.; Carroll, B. Yttrium Phosphate−Yttrium Vanadate Solid Solutions and Vegard's Law. *Inorg. Chem.* **1975**, *14*, 2199−2202.

(36) Wang, Z. W.; Daemen, L. L.; Zhao, Y. Z.; Zha, C. S.; Downs, R. T.; Wang, X. D.; Wang, Z. L.; Hemley, R. J. Morphology-Tuned Wurtzite-Type ZnS Nanobelts. *Nat. Mater.* **2005**, *4*, 922−927.

(37) Li, Z. P.; Liu, B. B.; Yu, S. D.; Wang, J. H.; Li, Q. J.; Zou, B.; Cui, T.; Liu, Z. X.; Chen, Z. Q.; Liu, J. The Study of Structural Transition of ZnS Nanorods Under High Pressure. *J. Phys. Chem. C* **2011**, *115*, 357−361.

(38) Yang, X. Y.; Wang, Y. N.; Wang, K.; Sui, Y. M.; Zhang, M. G.; Li, B. B.; Ma, Y. M.; Liu, B.; Zou, G. T.; Zou, B. Polymorphism and Formation Mechanism of Nanobipods in Manganese Sulfide (MnS) Nanocrystals Induced by Temperature or Pressure. *J. Phys. Chem. C* **2012**, *116*, 3292−3297.

(39) Xiao, N. R.; Zhu, L.; Wang, K.; Dai, Q. Q.; Wang, Y. N.; Li, S. R.; Sui, Y. M.; Ma, Y. M.; Liu, J.; Liu, B. B.; Zou, G. T.; Zou, B. Synthesis and High-Pressure Transformation of Metastable Wurtzite-Structured $CuGaS_2$ Nanocrystals. *Nanoscale* **2012**, *4*, 7443−7447.

(40) San-Miguel, A. Nanomaterials Under High-Pressure. *Chem. Soc. Rev.* **2006**, *35*, 876−889.

(41) Wang, Z. W.; Guo, Q. Size-Dependent Structural Stability and Tuning Mechanism: A Case of Zinc Sulfide. *J. Phys. Chem. C* **2009**, *113*, 4286−4295.

(42) Quan, Z. W.; Wang, Y. X.; Bae, I. T.; Loc, W. S.; Wang, C. Y.; Wang, Z. W.; Fang, J. Y. Reversal of Hall−Petch Effect in Structural Stability of PbTe Nanocrystals and Associated Variation of Phase Transformation. *Nano Lett.* **2011**, *11*, 5531−5536.

(43) Yu, M.; Lin, J.; Wang, S. B. Effects of x And R^{3+} on The Luminescent Properties of Eu^{3+} in Nanocrystalline $YV_xP_{1-x}O_4:Eu^{3+}$ and $RVO_4:Eu^{3+}$ Thin-Film Phosphors. *Appl. Phys. A: Mater. Sci. Process.* **2005**, *80*, 353−360.

(44) Moura, M. R.; Ayala, A. P.; Guedes, I.; Grimsditch, M.; Loong, C. K.; Boatner, L. A. Raman Scattering Study of $Tb(V_{1-x}P_x)O_4$ Single Crystals. *J. Appl. Phys.* **2004**, *95*, 1148−1151.

(45) Wang, Z. W.; Wen, X. D.; Hoffmann, R.; Son, J. S.; Li, R. P.; Fang, C. C.; Smilgies, D. M.; Hyeon, T. Reconstructing A Solid-Solid Phase Transformation Pathway in CdSe Nanosheets with Associated Soft Ligands. *Proc. Natl. Acad. Sci. U.S.A.* **2010**, *107*, 17119−17124.

(46) Panchal, V.; Manjón, F. J.; Errandonea, D.; Rodríguez-Hernández, P.; López-Solano, J.; Muñoz, A.; Achary, S. N.; Tyagi, A. K. High-Pressure Study of $ScVO_4$ by Raman Scattering and ab Initio Calculations. *Phys. Rev. B* **2011**, *83*, 064111−1−064111−10.

18612

dx.doi.org/10.1021/jp405405t | *J. Phys. Chem. C* 2013, 117, 18603−18612